

Numerical simulation of ultrafast expansion as the driving mechanism for confined laser ablation with ultra-short laser pulses

Jürgen Sotrop · Alfred Kersch · Matthias Domke ·
Gerhard Heise · Heinz P. Huber

Received: 30 April 2013 / Accepted: 4 July 2013 / Published online: 6 August 2013
© Springer-Verlag Berlin Heidelberg 2013

Abstract Recently, a so-called “directly induced” laser ablation effect has been reported, where an ultra-short laser pulse (660 fs and 1053 nm) irradiates a thin Mo film through a glass substrate, resulting in a “lift-off” of the irradiated layer in form of a thin, solid, cylindrical fragment. This effect provides a new and very energy-efficient selective structuring process for the Mo back electrode in thin-film solar cell production. To understand the underlying physical mechanisms, a 3D axisymmetric finite element model was created and numerically solved. The model is verified by a direct comparison of experimental and numerical results. It includes volume absorption of the laser pulse, heat diffusion in the electron gas and the lattice, thermal expansion of the solid phase and further volume expansion from phase transition to fluid and gas, and finally the mechanical motion of the layer caused by the resulting stress wave and the interaction with the substrate. The simulation revealed that irradiation of the molybdenum layer with an ultra-short pulse causes a rapid acceleration in the direction of the surface normal within a time frame of a hundred picoseconds to a peak velocity of about 100 m/s. The molybdenum layer continues to move as an oscillating membrane, and finally forms a dome after about 100 ns. The calculated strain at the edges of the dome exceeds the tensile stress limit at fluences that initiate the “lift-off” in experimental investigations. In addition, the simulation reveals that the driving mechanism of the “lift-off” is the ultrafast expansion of the interface layer and not the generated gas pressure.

1 Introduction

To reduce ohmic losses, modules of thin-film solar cells need to be separated in serially interconnected sub-cells [1–10]. The state of the art monolithic serial interconnection of CIGS (Copper-Indium-Gallium-Diselenide) thin-film solar cells involves a structuring process, where a Mo p-contact is galvanically separated with nanosecond laser ablation by illuminating the molybdenum layer from the front side and evaporating the metallic volume completely [11, 12]. This direct laser ablation process utilizes an excess of energy and produces burr and micro cracks. With an ultrafast laser, however, a “directly induced” laser ablation or “lift-off” process is initiated if the layer is illuminated from the glass substrate back side. As a result, the film is removed in form of a solid disc [13, 14]. This is an attractive alternative for industrial application with several advantages: The structure of the ablation is free from burrs without thermal side effects on the molybdenum film and the coated substrate. Based on partial melting or evaporation, the removal is very energy-efficient. Compared to the total evaporation enthalpy of Mo, which is 78 J/mm^3 , the energy per ablated volume is only 30 J/mm^3 [15, 16]. Together with the single pulse removal capability of the complete layer, high speed processing is possible. To further optimize this process for industrial applications or to transfer the method to other laser processes or materials, such as LIFT [17, 18], blister formation [19, 20], rapid prototyping of bio sensor chips [21] or opening of dielectric layers in silicon photovoltaics [22–24], it is necessary to understand the physical mechanisms behind the “directly induced” laser ablation in detail.

There have been several attempts to investigate similar ablation processes with experimental and numerical simulation studies. For induced laser interaction with nanosecond

J. Sotrop (✉) · A. Kersch · M. Domke · G. Heise · H.P. Huber
Munich University of Applied Sciences, Lothstrasse 34, 80335
Munich, Germany
e-mail: jsotrop@hm.edu
Fax: +49-0-8912651603

pulse duration, the observed effects are related to a vapour or plasma phase, which provides the gas or plasma pressure as the driving force.

An experimental investigation of the pressure generated by nanosecond-pulses in the confined interface between transparent substrate and a thick metallic absorber for laser shock processing was performed by Fabbro et al. [25]. The driving force for the shock wave formation was related to the generation of a confined plasma.

Adrian et al. [26] investigated the laser induced forward transfer (LIFT) process, where a 15-ns laser pulse, which is irradiated through the backside of a transparent substrate, ejects a 1- μm -thick metallic film from the front side and deposits the material on a target. A 1D simulation model calculated the temperature profile with the result that the supplied laser energy was more than sufficient to melt and partially evaporate the material. The conclusion was that the force for ejection should result from the vapour pressure of the partially vaporized metal.

Kattamis et al. [27] simulated a polyimide μm -film blister formation for LIFT with 40-ns pulse duration. The only driving force for the blister formation was explained by the pressure of an ideal gas and an adiabatic expansion. During the volume work the gas was still heated by the laser energy and increased the pressure value.

For femtosecond laser processing the observed effects are initiated by ultrafast heating or melting, which produce shock waves, leading to a delamination. The gas pressure plays only a minor role for the ablation, due to the short time interval of energy deposition and the short time interval provided for the vapour phase followed by immediate condensation.

To further explore the mechanism behind absorption, Itina et al. [28] simulated the impact of ultra-short 100-fs pulses on a metallic bulk with a 1D multiphysics model including a two-temperature model and a hydrodynamic model with a volume as a function of pressure. The solution of the equation yielded shock waves with velocities of several km/s. The ablation effect was explained by a compressive shock wave propagating into the bulk while the unloading rarefaction wave leads to the material expansion or removal.

That mechanical stress from thermal expansion of solid material in contrast to vapour pressure from a heated gas can be a major driving force in an ablation process was revealed by Ivanov et al. [29] in a theoretical work using a fundamental molecular dynamics simulation based on interatomic interaction. The simulation explains the formation of nanobumps in 20-nm Ni films on glass as the result of an acceleration of the thin film away from the substrate, caused by compressive stress up to 8 GPa created from thermal expansion and a subsequent plastic deformation of the material. The simulation however assumes a perfectly rigid substrate

as the mechanic boundary condition implying an elastic reflection of the expanding film from the substrate and leading to a very high take-off speed of 300 m/s.

In a work by Shugaev et al. [30] the stress waves created from thermal expansion were investigated with a multiphysics continuum model including a two-temperature model and a continuum elastic model in 1D. The simulation analysed the very first stage of LIFT processes for 200-fs pulses on 40-nm films of Au, Cr and Zn to find out why the material is ejected in different phase compositions. The result shows that with the same fluence of 0.35 J/cm² different electron gas and lattice temperatures are reached and that e.g. for gold the ejected material is only partially molten, in agreement with cited experimental work. The driving force was explained by a formation of strong pressure waves caused by instantaneous laser induced heating and subsequent unloading from the side of the free film boundary.

Zergioti et al. [31] made a comparative study of the effect of ultra-short (0.5 ps) and short (30 ns) pulses on the laser forward transfer of 40-nm Cr-films on glass. In case of fs laser pulses, a shock assisted removal was observed. An induced high pressure gradient by the fs laser, lead to a shock wave in the direction of the Cr air-side followed by a rarefaction wave propagating in the opposite direction. When the rarefaction wave reached the substrate film interface, the Cr layer was removed.

Recently, we published an analytical model to describe the bulging and ablation behaviour of a thin Mo film [15, 16]. The laser energy is absorbed in a fraction of the layer volume defined by the optical penetration length. This irradiated volume is fully evaporated, followed by an adiabatic expansion of the confined vapour and hydrostatic pressure is created. Ablation occurs when the shear stress at the edges exceeds some limit. The calculated energies needed to enable these processes are four times lower than the measured ones. But in the model we had to neglect shock waves, phase transitions and thermal expansion. Consequently, numerical simulation is the only way to calculate their contribution to the ablation process.

In the current paper we want to find out with modelling and simulation why the molybdenum layer can be removed so efficiently. In our simulation the parameters as well as the space and time scale are chosen to allow a comparison between a multiphysics model and the experimental results of the “directly induced” laser ablation [32–35]. The ultrafast laser pulses in these experiments of 660 fs is applied through a glass substrate to the 435-nm-thick molybdenum layer with low fluence from 0.4 to 0.6 J/cm². The threshold to ablate this layer completely is around 0.6 J/cm² which outperforms the processes in the cited articles [36–40] that report on direct laser ablation in terms of energy efficiency by far.

Now, in this paper we present a 3D axisymmetric, transient multiphysics model of the “directly induced” laser ablation for the complete process involving the following effects: the absorption of the laser pulse in the metallic layer by the electrons; the dissipation and the heat transfer to the lattice; the heating and phase transition in the metallic film; the propagation of a melt and evaporation front; the heat dissipation inside the layer and to the adjacent material; the thermo-elastic and elasto-mechanic reaction of the material leading to a mechanical interaction with the substrate and finally an acceleration of the partially intact layer; the plastic deformation of the material under temperature and stress and, last, the motion of the layer leading to membrane oscillations, shear forces and strain.

2 Physical model and simulation methods

2.1 Model assumptions

The object to be irradiated consists of a thin molybdenum layer which is vacuum coated on a glass substrate, shown in Fig. 1. The glass is nearly transparent for the wavelength of 1053 nm. Since the laser intensity distribution is axial symmetric (Table 1), we can simplify the geometry to the radial-vertical projection plane. As simulation domain we choose a rectangular molybdenum layer section with a height of 435 nm and a radius of 30 μm . The molybdenum layer beyond this radius, the glass substrate and the air outside this domain is modelled with appropriate boundary conditions. In the geometry of Fig. 1 the ablating molybdenum layer will move in the downward direction.

The whole ablation process is divided into eight steps (Fig. 2a–h):

- Irradiation through the glass substrate, partial reflection and absorption by the electron gas;
- Heating of the electrons, thermal diffusion and heat transfer to the molybdenum lattice;
- Thermal diffusion and thermal expansion of the heated solid molybdenum;
- Additional thermal expansion at the phase transition from solid to liquid;
- Emergence of vapour pressure in the interface between glass and molybdenum layer;
- Mechanical deformation of the molybdenum layer;
- Interaction of layer and substrate leading to acceleration of layer;
- Radial stress from plastic deformation and shearing, if strain limit is exceeded.

The physical assumptions to describe these steps are as follows:

Table 1 Laser beam parameters

Variable	Symbol	Value	Unity
Wavelength	λ	1053	nm
Pulse duration @ FWHM	T_p	660	fs
Beam radius @ e^{-2}	w_0	21	μm
Fluence in simulation	Φ_0	0.40–0.55	J/cm^2

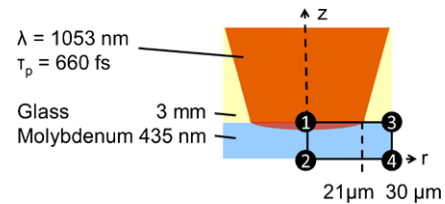


Fig. 1 The thin-film molybdenum layer is irradiated (660 fs, 1053 nm) through a transparent glass. Only the rectangular domain is used in the model. Important points at the boundary of the axisymmetric simulation domain are numbered from 1 to 4. The maximum irradiated intensity is reached in the centre at point 1. The distance from 1 to 3 is 30 μm and from 1 to 2 is 435 nm.

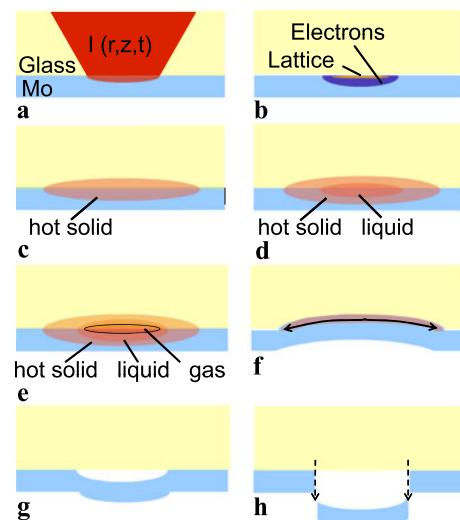


Fig. 2 Physical model of the ablation process. (a) A fraction of the laser pulse (660 fs, 1053 nm) energy is absorbed by the free electrons. (b) These diffuse thermally and heat up the lattice by relaxation. (c) The solid expands thermally. (d) The molybdenum is partially melted with additional thermal expansion due to melting. (e) Finally, a fraction of the melt becomes evaporated and vapour pressure rises. (f) The layer first expands in the normal direction to the glass and shock waves created from fast expansion interact with the substrate and the layer becomes accelerated. (g) The layer bulges and the material become strained in critical regions. (h) Either a dome is formed or the layer is ablated when a critical strain is exceeded

- The laser beam is focused on the molybdenum surface through the glass substrate with a radius of 21 μm . It is reflected of the glass surface as well as of the glass-molybdenum interface. The reflectivity of the whole

system has been measured as 50 % [41]. Hence only 50 % of the intensity is absorbed in the molybdenum volume near the surface. For molybdenum the absorption coefficient is known (see Table 2) and the optical penetration length with about 20 nm is much smaller than the thickness of the layer, such that interference effects are not present and the volumetric absorption can be described by a Lambert–Beer law.

- (b) The radiation is predominantly absorbed by the electron gas of the molybdenum layer. For the electrons, temperature, their heat capacity, the diffusion coefficient and the electron–phonon coupling is relevant. All these parameters are under debate, but we have used values from the recent literature (Table 2). The electrons diffuse and relax fast; in that way the energy is transferred to the solid lattice. The extension of the heated lattice region depends on the electron–phonon coupling coefficient which is chosen according to literature (Table 2).

The transition to mechanical motion is generated by three fundamental mechanisms with different quantitative contributions.

- (c) The first mechanism is the linear thermal expansion, due to the heating of the solid above room temperature. This raises a thermal expansion resulting in a compressive stress. The lattice thermal conductivity and expansion coefficient, as well as the solid thermodynamic properties of Mo, is well known (Table 3).

- (d) The second mechanism is an additional thermal expansion at the phase transition from solid to liquid, if the melting temperature is reached. The melting temperature and heat of fusion of molybdenum are known at zero pressure. But at the high compressive pressure and fast temperature ramp during the pulse, superheating effects can be expected. Lacking the knowledge about the equation of state we use the equilibrium melt temperature in our model. For the additional volume expansion during the melting, we use experimental values [42]. These values as well have been obtained under near equilibrium conditions. The melting temperature is an important parameter in our model since we assume that the interface between liquid metal and substrate has a reduced cohesive force, hence that the maximum extension of the liquid interface defines the ablation radius.
- (e) The third mechanism is the pressure generated by the vaporized molybdenum, possibly relevant above the evaporation temperature. If a gas is generated, it needs some time to reach the vapour pressure such that its value can be considered as an upper limit of the effect. The vapour pressure is essentially well known (Table 4).
- (f) To create mechanical motion of the film, several mechanisms may be relevant. First, the rapid increase of compressive stress creates stress waves close to the interface which partially reflect and travel in normal direction. In other words, the expansion causes recoil pressure. These effects require a transient continuum elastic description in the normal direction. The momentum exchange with the substrate furthermore requires a proper treatment of its continuum elastic properties. Overall the molybdenum may finally get an initial velocity in the normal direction, when there is some counteracting force from the substrate back to the layer. Second, because the molybdenum layer expands first close to the interface below the neutral fibre of the layer considered as rigid plate, the layer bends towards the direction of the glass to lower its potential energy, similar to the bimetallic strip effect. Such an effect requires an inclusion of the

Table 2 Electronic data of molybdenum [47, 49]

Variable	Symbol	Value	Unit
Electron–phonon coupling constant	G	$13 \cdot 10^{16}$	(W/m ³ K)
Lattice heat conductivity	k_0	135	(W/(m K))
Specific electron heat constant	γ	$34 \cdot 10^{-3}$	J/(kg K ²)
Electronic heat conductivity	k_e	$k_0 \frac{T_e}{T_l}$	W/(m K)
Electronic heat capacity	C_e	γT_e	J/(kg K)
Absorption coefficient @ 1053 nm	α_{Mo}	$5.23 \cdot 10^7$	1/m

Table 3 Parameters for the heat capacity model [50]

Variable	Symbol	Value	Unity
Heat capacity molybdenum	a	250	J/(kg K)
Norm factor gauss function melting	b	$\frac{1}{50\sqrt{2\pi}}$	1
Melting temperature	T_m	2896	K
Melting enthalpy	ΔH_M	$389 \cdot 10^3$	J/kg
Norm factor gauss function evaporating	c	$\frac{1}{50\sqrt{2\pi}}$	1
Vaporization temperature	T_v	4912	K
Vaporization enthalpy	ΔH_V	$6.25 \cdot 10^6$	J/kg
Width of Gaussian latent heat model (FWHM)	ΔT	50	K
Thermal expansion coefficient	α_{exp}	$4.8 \cdot 10^{-6}$	1/K

Table 4 Material data of molybdenum [50]

Variable	Symbol	Value	Unit
Mass density	ρ	10280	kg/m ³
Young’s modulus	E	321	GPa
Yield stress level	σ_{Yield}	0.3	GPa
Kinematic tangent modulus	E_{Tkin}	1	GPa
Vapour pressure @ 2742 K	P_{Vapour}	1	Pa

radial direction into the continuum elastic model. The ablation may finally happen when the initial velocity of the layer is sufficient to overcome the potential energy barrier of the layer under the non-uniform compression.

- (g) When the layer has succeeded to detach from the substrate the motion of the layer away from the substrate continues. Compared to the velocity of the shock waves, the centre of mass velocity is probably much smaller such that the film will solidify and acquire a homogeneous temperature during motion. Then the radial stress from expansion in the radial direction becomes the only driving force except possibly a residual vapour pressure. Furthermore the layer is still fixed beyond the ablation radius. Again, the inclusion of the stress in the radial direction is necessary to describe this stage of motion.
- (h) The inertial forces together with the compressive force in the radial direction and the cohesive forces outside the ablation radius determine the shear stress in the layer. When some critical value is exceeded, the layer will be damaged or detached, depending on the damage. If the critical value is not exceeded, the layer keeps attached, but may be plastically deformed. Otherwise an elevated dome could not stably exist. Therefore the inclusion of plastic material properties is necessary to reproduce a dome in the simulation. Since the layer does not consist of bulk molybdenum with known literature material properties (Table 4) but a sputtered, less dense, anisotropic material, some uncertainties are introduced at this point. Especially the plastic deformation behaviour can be expected to be different than in a pure solid. We model the linear elastic regime with the solid properties of the temperature-dependent Young’s modulus and chose the yield stress level as 300 MPa (Table 4). The elastic properties of the fluid Mo is approximated with compressibility close to the Young’s modulus and a liquid-like Poisson ratio of close to 0.5. Furthermore, we expect the layer to shear off in our model when a critical strain is exceeded.

2.2 Mathematical model

For the simulation we formulate the different physical processes in a set of coupled partial differential equations

and solve them numerically with a finite element method using the software “Comsol Multiphysics” [43].

2.2.1 Absorption of the laser pulse

The laser pulse defines a volumetric heat source, Eq. (2.1). We assume a Gaussian intensity distribution in radial direction, exponential decay in axial direction according to the Lambert–Beer law and a sech^2 pulse shape in the time domain.

$$Q(r, z, t) = (1 - R) \frac{1.76\Phi_0}{2\tau_p} e^{-\frac{2r^2}{w_0^2}} \alpha e^{-\alpha z} \times \text{sech}^2\left(\frac{1.76(t)}{\tau_p}\right) \left[\frac{\text{W}}{\text{m}^3}\right] \tag{2.1}$$

Here, R is the reflectivity, $(1 - R)$ the absorbed fraction of the laser intensity, Φ_0 the peak fluence, w_0 the beam radius at e^{-2} intensity level, α the absorption coefficient, r the radial spatial coordinate, z the axial spatial coordinate, t the time and τ_p the pulse duration as full width half maximum value (FWHM).

2.2.2 Thermal heat diffusion by the two-temperature model and latent heat effects

To get a space and time diffusion of the electron and lattice temperature in the molybdenum layer, the two-temperature model [44–48] is applied. The heating is described by two heat diffusion equation for electrons (Eq. (2.2)) and for the lattice (Eq. (2.3)). The heat of melting and evaporation of the lattice is included in the temperature dependence of the specific heat capacity, shown in Eq. (2.4). We approximate this dependence with a Gaussian function of finite width ΔT centred around the melting temperature T_M and the evaporation temperature T_V instead most correctly with a delta function to make the model numerically solvable (Table 3, Fig. 3). The heat of evaporation for molybdenum ΔH_V is approximately 16 times higher than the heat of melting ΔH_M . For the liquid specific heat we choose the same value than for the solid material.

$$\rho C_e(T_e) \frac{\partial T_e}{\partial t} = \nabla(-k_e(T_e)\nabla T_e) - G(T_e - T_l) + Q(r, z, t) \tag{2.2}$$

$$\rho C_l(T_l) \frac{\partial T_l}{\partial t} = \nabla(-k_l(T_l)\nabla T_l) + G(T_e - T_l) \tag{2.3}$$

$$C_l = a + \Delta H_M b e^{-\frac{1}{2}\left(\frac{T-T_M}{\Delta T}\right)^2} + \Delta H_V c e^{-\frac{1}{2}\left(\frac{T-T_V}{\Delta T}\right)^2} \left[\frac{\text{J}}{\text{kg K}}\right] \tag{2.4}$$

Here, T_e and T_l are electron and lattice temperatures, respectively, ρ is the mass density, C_e and C_l are the heat

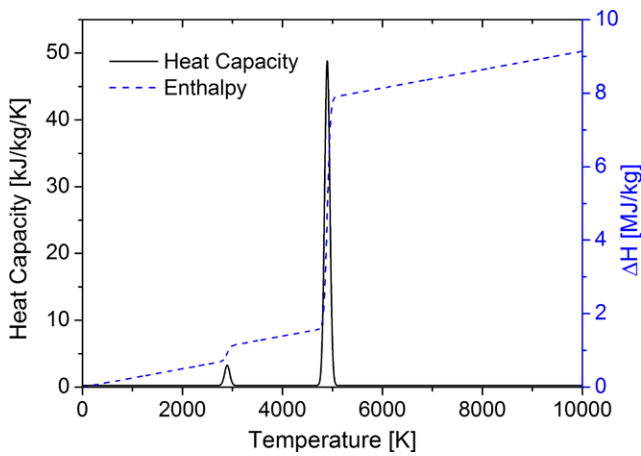


Fig. 3 Heat capacity and enthalpy vs. temperature. The latent heat for melting and evaporation is modelled by a Gaussian distribution.

capacities at constant pressure, k_e and k_l are the specific thermal conductivities and G is the electron–phonon coupling constant. The indices e and l label electron and lattice, respectively.

2.2.3 Mechanical model: from thermal expansion to mechanical movement

The mechanical motion of the molybdenum layer is subject to inertial forces, thermal and deformation stress in the volume, pressure and adhesion forces at the boundary, and leads to large and possibly nonlinear deformation. Moreover, plastic deformation will occur which will introduce damping effects on oscillatory motion.

The large deformation requires two coordinate systems: One is fixed in space and is the spatial frame and the second is fixed in the moving and deforming body and is the material frame. The dynamical equation of motion for a continuum with mass density ρ is the Cauchy–Green equation for the displacement \mathbf{u} subject to body forces \mathbf{F}_v and volume stress \mathbf{S} (Eqs. (2.5) and (2.6)). The stress \mathbf{S} is the 2nd Piola–Kirchhoff stress tensor which is the stress tensor $\boldsymbol{\sigma}$ in the material frame, transformed to the spatial frame, \mathbf{J} being the Jacobian of the coordinate transformation. In the material frame the stress \mathbf{S} is related to the strain tensor $\boldsymbol{\epsilon}$ and the thermal strain tensor $\boldsymbol{\epsilon}_{th}$ either with the Hooke law in the linear elastic regime, \mathbf{C} being the tensor of elastic constants of the material (Eqs. (2.7)–(2.9)), or with a plastic deformation model [51, 52].

$$\rho \frac{\delta^2 \mathbf{u}}{\delta t^2} - \nabla \mathbf{S} = \mathbf{F}_v \tag{2.5}$$

$$\mathbf{S} = \det(\mathbf{J})^{-1} \mathbf{J} \boldsymbol{\sigma} \mathbf{J}^T \tag{2.6}$$

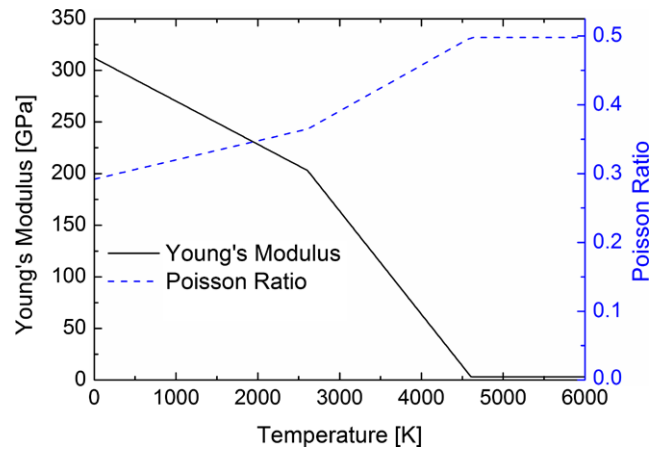


Fig. 4 Temperature-dependent Young’s modulus and the Poisson ratio [53]

$$\mathbf{S} = \mathbf{C} : (\boldsymbol{\epsilon} - \boldsymbol{\epsilon}_{inel}) - \left(\frac{\text{trace}(\mathbf{C} : (\boldsymbol{\epsilon} - \boldsymbol{\epsilon}_{inel}))}{3} + \mathbf{p}_w \right) \mathbf{I}$$

$$\mathbf{p}_w = -\frac{1}{3} \text{trace}(\mathbf{S}), \quad \boldsymbol{\epsilon} = \frac{1}{2} \left[(\nabla \mathbf{u})^T + \nabla \mathbf{u} + (\nabla \mathbf{u})^T \nabla \mathbf{u} \right]$$

$$\sigma_{mises} < \sigma_{ys0} \tag{2.7}$$

$$\boldsymbol{\epsilon}_{inel} = \boldsymbol{\epsilon}_{th} + \boldsymbol{\epsilon}_p, \quad \boldsymbol{\epsilon}_{th} = \boldsymbol{\alpha}(\mathbf{T} - \mathbf{T}_{ref}) \tag{2.8}$$

$$\sigma_{ys} = \sigma_{ys0} + \frac{\mathbf{E}_{Tkin}}{\mathbf{1} - \frac{\mathbf{E}_{Tkin}}{\mathbf{E}}} \frac{2}{3} \boldsymbol{\epsilon}_p, \quad \sigma_{mises} > \sigma_{ys0} \tag{2.9}$$

Young’s modulus and the Poisson ratio are implemented as temperature-dependent [53]. Young’s modulus is decreasing while the Poisson ratio is increasing with temperature, thus that the bulk modulus is nearly constant. Above the melting point, Young’s modulus becomes small, while the Poisson ratio approaches nearly 0.5 (Fig. 4). The yield stress level is set to 300 MPa only for the solid molybdenum. The plastic deformation model is used when the von Mises stress σ_{mises} exceeds a yield stress σ_{ys0} . In the plastic regime, $\boldsymbol{\sigma}$ depends linearly on $\boldsymbol{\epsilon}$ (with \mathbf{E}_{Tkin} the kinematic tangent modulus), but the strain freezes with an isotropic hardening model. Since $\boldsymbol{\sigma}$ raises only weakly in the plastic regime, we consider the strain as the quantity to monitor shearing. This kinematic, plastic material model is a compromise between the need to have stress in the vertical direction and the need to have stress relaxation in the radial direction. Finally, a Rayleigh damping term is added to the equation of motion. It is characterized by a velocity-dependent friction chosen to damp the shock waves on a nanosecond scale.

2.2.4 Thermal boundary conditions

For the electron temperature all boundaries are modelled as thermally insulating so that the heat is completely transferred to the lattice inside the domain. For the lattice temperature model, Fig. 5a gives an overview of the chosen ther-

Table 5 Thermal and elasto-mechanical boundary conditions (b.c.)

B.C.	Lattice temperature	Displacement
1	Axisymmetric	Axisymmetric
2	$-\mathbf{n}(k\nabla T) = 0$	Free
3	$-\mathbf{n}(k\nabla T) = Q_b$ $Q_b = -\lambda_{\text{eff}} \left(T \sqrt{\frac{\sigma c_p}{k\pi t}} + \frac{dT}{dt} \sqrt{\frac{\sigma c_p t}{k\pi}} \right)$	$\sigma \mathbf{n} = -\mathbf{k}_{\text{glass}}(\mathbf{u} - \mathbf{u}_0) - \mathbf{d}_{\text{glass}} \frac{\partial \mathbf{u}}{\partial t}$ Unidirectional inside and bidirectional outside melt radius
4	$-\mathbf{n}(k\nabla T) = q_0$ $q_0 = h(T_{\text{ext}} - T)$	$\sigma \mathbf{n} = -k_{\text{Mo}}(\mathbf{u} - \mathbf{u}_0)$

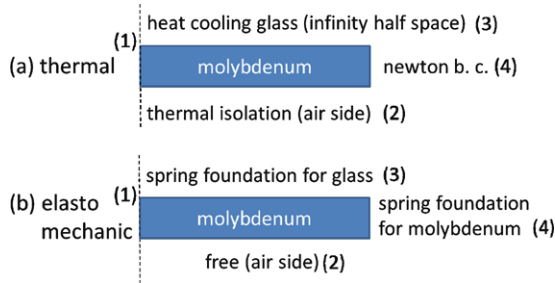


Fig. 5 Boundary conditions (a) for the thermal model and (b) for the elasto-mechanical model

mal boundary conditions. The symmetry axis and the boundary towards the air are treated as insulating. The boundary conditions at the interface to the metal and the glass substrate, however, are carefully selected to model the temperature evolution correctly, after the large temperature inhomogeneity within the film thickness has decreased. Then, after a nanosecond, the radial temperature distribution in the layer and the resulting forces depend on the heat losses to the outside regions. The boundary condition to the radially distant metal layer has been modelled as a Newton boundary condition. This is sufficient because the radial extension of the simulation domain is sufficiently large that the major fraction of the heat loss is to the glass. The boundary condition to the glass substrate is derived from the Green function of the heat equation with heat loss to an infinite half space defined by the thermal conductivity and heat capacity of glass. The thermal state of the half space is contained in the temperature gradient along the boundary. Additionally, a gap of width u between bulging metal and glass has been taken into account in the effective conductivity λ_{eff} . The accuracy of this boundary condition has been confirmed with a variety of test calculations containing the glass substrate in an extended domain instead of the boundary condition.

2.2.5 Mechanical boundary conditions

The mechanical boundary condition (Fig. 5b) is a crucial point of the model since it contains the interaction between

Table 6 Parameters for the boundary condition models

Variable	Symbol	Value	Unity
Effective heat conductivity	λ_{eff}	$\frac{0.5 \cdot 10^{-6} - u}{\left(\frac{0.5 \cdot 10^{-6}}{1.4}\right) + \left(\frac{-u}{0.03}\right)}$	W/(m K)
Spring constant glass	k_{glass}	$1.6 \cdot 10^6$	N/m
Damping factor glass	d_{glass}	$1.5 \cdot 10^7$	N s/(mm ²)
Spring constant molybdenum	k_{Mo}	10^{18}	N/(mm ²)
External temperature	T_{ext}	293.14	K
Heat transfer coefficient	q_0	$70 \cdot 10^6$	W/m ²

the expanding layer and the substrate, in other words, the recoil pressure. It introduces the dependence of the ablation process on the substrate’s elastic properties. Since the Young’s modulus of the glass substrate is smaller than of the metal layer, the substrate cannot be modelled as rigid boundary condition and a shock-wave will not be reflected completely. The counteraction back from the substrate to the layer may be weak. We chose to describe the substrate in the boundary condition with a spring model where the parameters of mass, spring constant and damping constant were calibrated carefully. The spring continuum obtains a value for deformation and velocity in every point along the boundary. The three parameters of that spring continuum model were calibrated to simulation, where the substrate has been included as an additional domain in contact to the layer and good agreement has been obtained. This spring model describes the response of the substrate to the layer material moving in substrate direction. A second spring model was used to describe the adhesion force of the layer outside the melt region. Inside the melt region no further spring modelling is applied; the layer is allowed to move away, when the velocity is sufficient to overcome a possible potential energy barrier in the stressed layer.

The mechanical boundary to the radial outside is also described by spring models with the purpose to tolerate some radial deformation.

Table 5 summarizes the boundary condition models and Table 6 the respective parameter values.

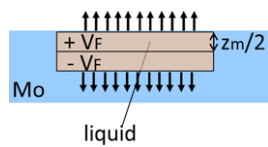


Fig. 6 The liquid area is divided in two segments, in which positive and negative volume forces are generated by the phase transition from solid to liquid

2.2.6 Modelling of the thermal expansion at the phase transition

At the phase transition from solid to liquid, the molybdenum gets an additional volume change of 5 %. According to data of Hixson and Winkler [42], this volume change occurs in a small temperature interval around the melting temperature. The direct implementation of this effect into a numerical model leads to volume expansion in a small spatial interval around the melt front. To avoid numerical instability and convergence problems we have implemented the thermal strain in “Comsol Multiphysics” effectively using a volume force model in which the expansion is smeared out over the whole melting zone. The melting zone is divided into two segments (rectangular in the axisymmetric projection). In the upper segment the force is directed in the direction to the glass, in the bottom segment the force is directed in the opposite direction. Equation (2.10) gives the magnitude of the volume forces, which cause a change of 5 % in the length and Fig. 6 shows the geometry. E is the Young’s modulus of molybdenum and $z_m/2$ is the height of each segment.

$$V_F = \pm \frac{2 \frac{\Delta l}{l} E}{\frac{z_m}{2}} \quad (2.10)$$

2.3 Meshing and time stepping

The mesh was selected as quadrilateral and structured, expanding from the centre point to the right bottom edge to map the strong physical gradients and the deforming mesh. For a fluence of 0.4 J/cm² the mesh consists of 2500 elements with an element ratio of 0.1 in axial and radial direction. For higher fluence of 0.5 and 0.55 J/cm², the mesh is refined to 10,000 elements with the same element ratio. To avoid numerical instabilities during nonlinear grid deformation we have modelled the mesh movement with an arbitrary Lagrangian–Eulerian algorithm.

The time integration uses an implicit method with an adaptive time step. For each time step the full set of coupled equations is solved with an iterative Newton solver. To meet the accuracy criterion the time step has to be around 10⁻¹⁵ s in the initial phase with large temperature and deformation gradients from shock waves. Because the temperature gradients are smoothed out and the shock waves are damped with the Rayleigh damping, the time step increases up to 10⁻⁹ s

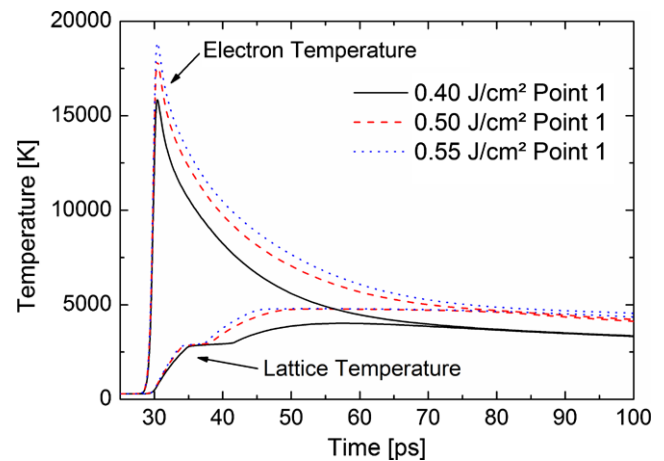


Fig. 7 Electron and lattice temperature at the centre for fluence of 0.40, 0.50 and 0.55 J/cm², pulse duration 660 fs, wavelength 1053 nm. Both temperatures have reached equilibrium after about 80 ps

during the calculation making the computational load of the temporal multiscale simulation acceptable. Fluence larger than 0.55 J/cm² requires more mesh elements and smaller time steps to achieve convergence and were not conducted for this investigation.

3 Simulation results

The multi-scale simulation was performed with fluence of 0.4, 0.5 and 0.55 J/cm². The evolution of the system is initiated by a laser pulse with the peak intensity shifted to 30 ps to comprise the rising slope. The edges of the simulation domain are numbered as shown in Fig. 1 for a facilitated presentation of the results. In point 1, the centre for the axisymmetric grid, the laser intensity reaches a maximum value. The distance from point 1 to point 3 is 30 μm. The radius of the laser pulse is 21 μm. The intensity at the boundary point 3 is about $e^{-4} \approx 1.8$ % of maximum intensity at point 1.

3.1 Absorption, electron heating, electron–phonon scattering, and phase transitions

The laser pulse is absorbed by the electrons leading to an electron peak temperature of ~19,000 K followed by the relaxation to the lattice. By comparing the electron and lattice temperature at a fluence of 0.40 to 0.55 J/cm² in point 1, the equilibrium is reached at a time of 80 to 100 ps (Fig. 7). The plateau visible in the lattice temperature at 35 ps is due to the latent heat of the melting. A second plateau becomes visible at 50 ps [54, 55] for a fluence of 0.50 and 0.55 J/cm² due to the latent heat of vaporization. But the melted and vaporized region is located close to the interface as becomes visible in Fig. 8 showing the lattice temperature at the points

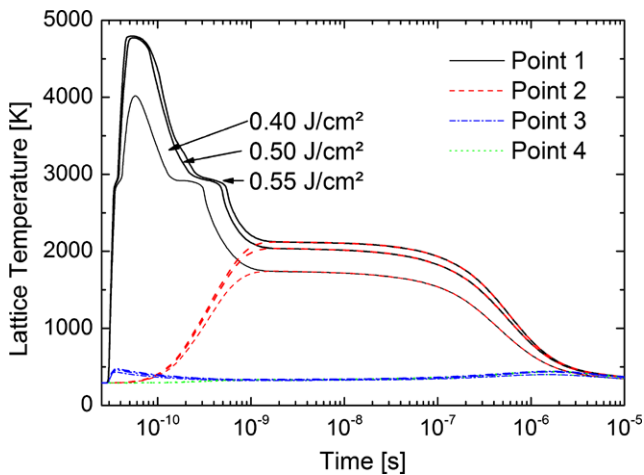


Fig. 8 Lattice temperature at the monitor points. Fluence 0.40, 0.50 and 0.55 J/cm². After around 400 ps the layer at point 1 is solidified; this is indicated by the ending of the temperature plateau. Time to reach a homogeneous temperature in vertical direction is about 1 ns. Outer points 3 and 4 are only slightly heated up to 500 K. Room temperature is reached after about 10 μ s

1 to 4. The time to reach a nearly homogeneous temperature in the layer in vertical direction is about 1 ns. Before this time after around 400 ps the layer is already solidified; this is indicated by the ending of the temperature plateau. The outer points 3 and 4 are only slightly heated up to 500 K. In the time frame from 1 ns to 10 μ s the solid molybdenum layer is cooled down to nearly initial room temperature for all described values of fluence. The melting depth is 90, 110 and 120 nm for 0.40, 0.50 and 0.55 J/cm², respectively.

3.2 Acceleration of the molybdenum layer

The lattice temperature reaches the vaporization temperature at 50 ps (see Fig. 7, lattice temperature point 1 at 0.55 J/cm²), and thus 20 ps after the intensity maximum of the laser pulse. Figure 9 shows the comparison between the resulting vapour pressure, determined at the temperature of point 1 (left y-axis), and the mean vertical pressure, averaged over the vertical direction from point 1 to 2 in the molybdenum film (right y-axis), for a fluence of 0.55 J/cm². The maximum vapour pressure of 75 kPa is reached at about 54 ps and nearly vanishes after about 150 ps due to condensation. In contrast, at 40 ps the mean vertical pressure already reaches a minimum of -2 GPa, which is related to compressive stress, caused by the thermal expansion during ultrafast heating and melting. Figure 10 shows the average acceleration (averaged over the vertical direction from point 1 to 2) of the entire film in dependence on time. A maximum acceleration was calculated to be $1.2 \cdot 10^{12}$ m/s², which corresponds to an acceleration of 10^{11} multiple of g at 40 ps. This results from thermal expansion during heating and at the phase transition from solid to liquid. Consequently,

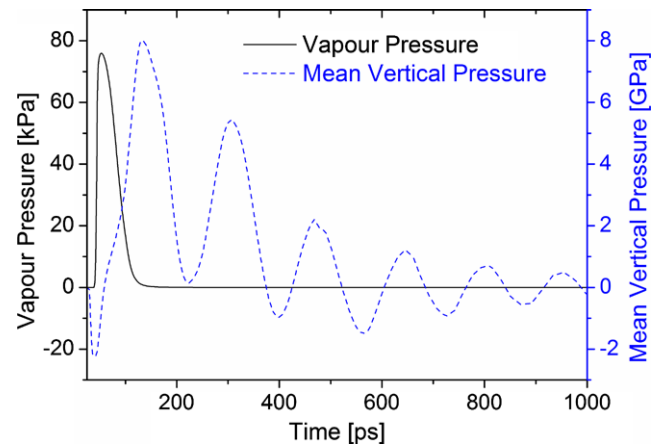


Fig. 9 Vapour pressure (determined at the temperature of point 1) and mean vertical stress component (averaged over the vertical direction from point 1 to 2) for a fluence of 0.55 J/cm². Vapour pressure does not exceed 75 kPa and has nearly vanished after 100 ps. The average vertical stress component is initially compressive (negative) and then reaches values up to 8 GPa. After the layer has detached from the substrate, the sign is alternating and is related to the thickness oscillation of the layer triggered by the expansion shock

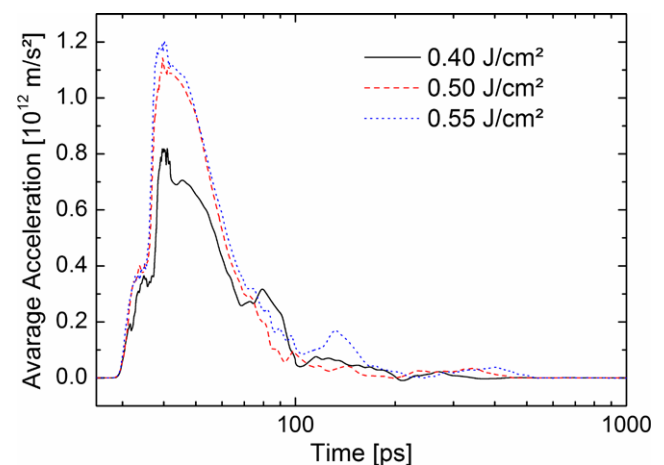


Fig. 10 Average acceleration (averaged over the vertical direction from point 1 to 2) in the centre for fluence of 0.40, 0.50 and 0.55 J/cm². First the layer accelerates by thermal expansion and the following backward impulse of the substrate in the order of 10^{11} multiple of g for all values of fluence. If the Mo layer is uncoupled from the glass substrate at 130 ps, the acceleration and therefore the external force is nearly zero

the simulation suggests that the acceleration of the film is mainly driven by ultrafast heating and melting and not by partial evaporation, as assumed in our earlier model [16]. This result is also supported by experimental observations of shock waves in the glass substrate, which are initiated by ultrafast heating and melting [56].

The physical mechanisms that lead to the acceleration of the molybdenum film are revealed in detail in Fig. 11. The displacements of points 1 and 2 relative to the initial position are plotted against time. First, the molybdenum is heated

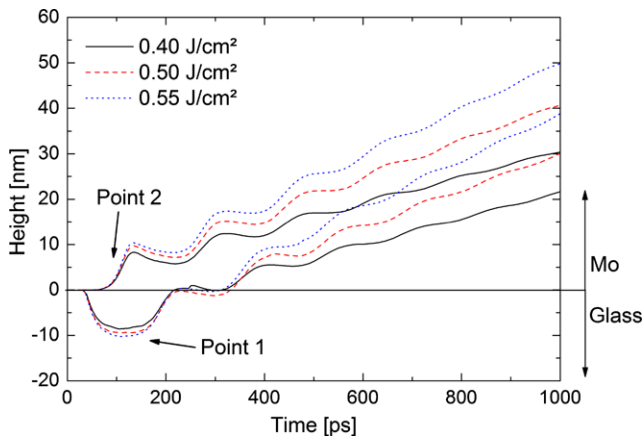


Fig. 11 The displacement of points 1 and 2. The glass is only in contact with the molybdenum in the first 130 ps. Then the molybdenum is propagating free within the area of the melting diameter. A shock-wave travels between the upper and lower boundary with the speed of sound of about 5800 m/s. This leads to a period of approx. 200 ps. We assumed a damping of the oscillation after the interaction with the substrate to model the observations and facilitate the multi-scale simulation. After about 1 ns points 1 and 2 have equal slopes for each fluence, indicating a different velocity for each fluence

by the laser pulse in point 1 at the molybdenum/glass interface and starts to expand. After 100 ps, point 1 has extended about 10 nm into the glass substrate whereas point 2 is still resting. Due to the spring model for the glass substrate, point 1 is pushed into the glass and the reset force of the glass creates an impulse which accelerates the layer away from the substrate. Thereby, the mean vertical pressure in Fig. 9 indicates high compressive strain that increases up to 8 GPa. At about 130 ps the molybdenum is uncoupled from the glass along the maximum melt radius. At the same time a shock-wave has propagated with the speed of sound of about 5800 m/s through the entire molybdenum layer and displaces point 2 by about 10 nm. The shock-wave is reflected and reaches point 1 at about 230 ps. Thus, point 1 seems to rest at the position of 0 nm displacement for about 100 ps. In fact, the acceleration of the centre of mass was already completed after the detachment at around 130 ps and the entire layer is in motion.

In the following, the oscillations of the moving layer are damped. The parameter of the damping, however, was chosen without affecting the initial acceleration and was not deduced from the parameter for plastic deformation. After about 1 ns points 1 and 2 have equal velocities for each fluence, which means the Mo layer is propagating nearly free at a constant speed.

3.3 Ultrafast heating and melting as driving forces

As described above, the “lift-off” is initiated by ultrafast heating and melting. The contribution of both effects on the bulging velocity of the dome can be analytically estimated.

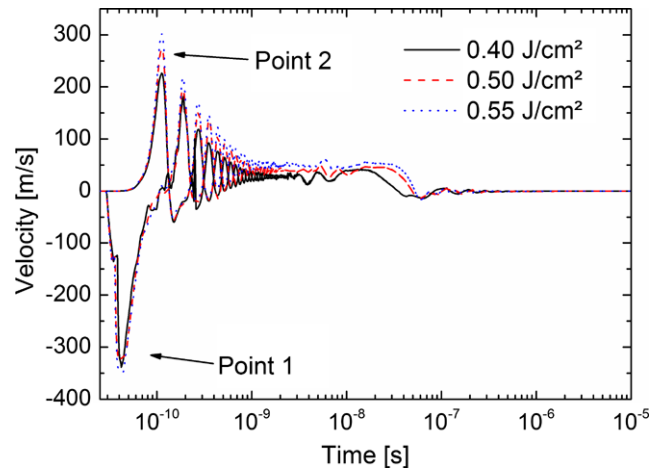


Fig. 12 Velocity over time in points 1 and 2 for fluence of 0.40, 0.50 and 0.55 J/cm². Point 1 travels with maximum speed into the glass, because of the assumed Rayleigh damping. Then points 1 and 2 oscillate inversely phased around the mean velocity

The initial velocity Δv that is caused by ultrafast heating can be estimated by

$$\Delta v = l\alpha \frac{\Delta T}{\Delta t}, \quad (3.1)$$

where the temperature difference ΔT is 4000 K, the heating time Δt is 20 ps, the heated layer thickness is 100 nm, and thermal expansion coefficient is $4.8 \cdot 10^{-6} \text{ m}^{-1}$. Hence, the resulting expansion velocity of the layer is about 100 m/s.

In addition, ultrafast melting causes a volume expansion at the phase transition to a liquid, which has been determined to be 5 % [42] (Fig. 1d). This expansion adds to the thermal expansion of the solid and accelerates the molybdenum layer further in axial direction. The velocity is determined by

$$v = \frac{\Delta l}{\Delta t} = \frac{l \cdot 0.05}{\Delta t} \quad (3.2)$$

For a melting depth Δl of 20 nm and a 5 % relative volume change with a melting time Δt of 5 ps, the resulting velocity is 200 m/s. This is twice the velocity from linear thermal expansion, caused by ultrafast heating.

The sum of both thermal expansion effects explains the magnitude of the initial velocity of point 1, which is 300 m/s in the direction to the glass, as shown in Fig. 12. The figure shows the velocity in point 2 as well which is directed away from the glass in response to the velocity in point 1. The relative velocity of point 1 in the direction to the glass is maximal, because of the Rayleigh damping.

3.4 The bulging process and dome formation at low fluence

The ultrafast acceleration causes the molybdenum to bulge and leads to a dome formation at low fluence, as shown in Fig. 13. For the motion of the membrane itself, the averaged velocity in axial direction over the layer thickness is

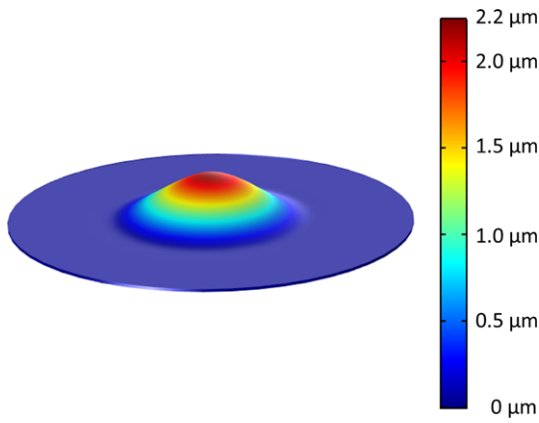


Fig. 13 Membrane height for 0.55 J/cm² during motion at 52 ns, measured from the Mo surface

the relevant quantity. The average velocity (averaged over the vertical direction from point 1 to 2) is essentially constant and directed away from the substrate during the last contact with the glass at about 130 ps until the motion slows down after 40 ns, as shown in Fig. 14. The average velocity is much smaller than the peak velocities in the shock wave and is the result of the damped back-reaction of the substrate on the layer. The deviations of the average velocity from a constant value in the centre are related to an oscillating motion of the moving membrane excited in several modes as well as membrane corrugation.

Figure 15 shows the centre dome height, measured from the Mo surface, as a function of time. The maximum height of 2.2 μm for a fluence of 0.55 J/cm² coincides with the time of deceleration of the membrane motion at about 40 ns. At the maximum height corrugation occurs, due to the strong initial shock-wave driven acceleration. After 400 ns, the frequency of the membrane oscillation is about 11 MHz, indicating a dynamic effect. This is followed by an oscillation, while the dome is shrinking with decreasing temperature. For a purely elastic material, the dome would shrink to zero height. But for the plastic material in our model we obtain a residual deformation defining the static height of the dome. We have mentioned already that the material properties of the sputtered molybdenum are not well characterized. The used plastic material model parameters have to be considered as estimates leading qualitatively to the observed dome height by Domke et al. [32].

The cooling of the film leads to a shrinking of the layer. Hence, the thermal expansion in radial direction has a significant contribution to bulging. Assuming a circular dome geometry, the maximum static dome height *h* caused by thermal expansion can be calculated (Table 7).

The temperature is taken at the time of maximum dome height. However, this is only a static view without plastic deformation and dynamic effects. In comparison, the simulation returns a maximum dome height of about 2.2 μm for a

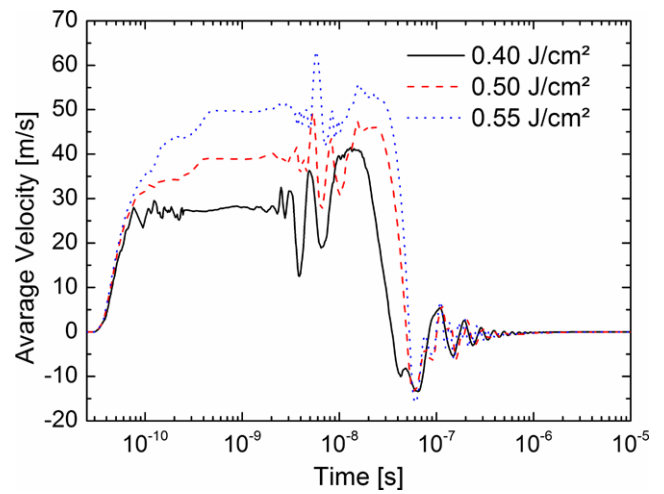


Fig. 14 Average velocity (averaged over the vertical direction from point 1 to 2) for fluence of 0.40, 0.50 and 0.55 J/cm². In the first hundreds of picoseconds the layer accelerates to a constant velocity. The oscillations at around 10 ns are numerical discretization errors. The oscillation at 100 ns is observed also in our height experiments and can be interpreted as corrugation. After 1 μs the mechanical motion has terminated

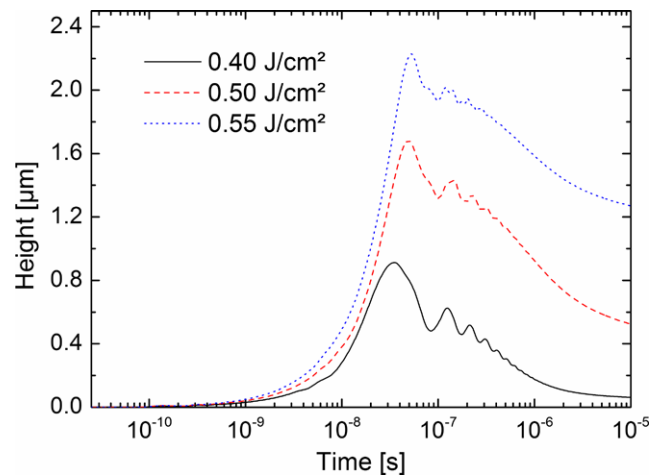


Fig. 15 Height of the dome for fluence of 0.40 J/cm², 0.50 J/cm² and 0.55 J/cm², measured from the Mo surface. The layer expands at constant bulging velocity and starts to oscillate after the maximum is reached, due to inertial effects. At the end of the timescale the layer has an irreversible deformation, although it cools down to room temperature. This is an effect of the plastic deformation

Table 7 Estimated maximum static dome height by thermal expansion for a circular dome geometry

Fluence [J/cm ²]	ΔT [K]	Maximum static dome height <i>h</i> [nm]
0.40	1300	970
0.50	1490	1050
0.55	1585	1070

fluence of 0.55 J/cm^2 . Thus, the contribution of radial thermal expansion to the bulging of the dome is expected to be below 50 %. The other contribution is calculated from plastic deformation and inertia overshoot.

3.5 Shearing from strain and threshold to ablation at high fluence

The motion of the membrane away from the substrate creates stress and strain in the layer. Since we have implemented a plastic deformation model, the stress relaxes with time. The strain values, however, are not reduced from plastic deformation and are better suited to identify a condition for fracture. Figure 16 shows the maximum values for radial strain over the radial position as function of time for a fluence of 0.40 and 0.55 J/cm^2 . The maximum value is located at the melting radius and increases strongly with the fluence. It can be expected, that a critical value is exceeded for some fluence and that fracture of the layer occurs along the periphery, leading to the “lift-off” ablation with a layer fragment in form of a disk. However, the strain at the centre (radius 0) also increases with the fluence. This could lead to a crack in an ablated dome, as described by Heise et al. [16].

4 Discussion

4.1 Analysis of the driving force for the initiation of the “lift-off”

In literature there are several explanations for the driving forces that initiate the laser “lift-off” by confined ablation. Especially, if ultra-short pulse lasers are used, ultrafast effects might also be involved [28–31]. In our simulation, we considered four effects:

1. Expansion of gas under confinement
2. Thermal expansion in axial direction driven by ultrafast heating
3. Thermal expansion in axial direction driven by ultrafast melting during the phase transition from solid to liquid
4. Thermal expansion of the heterogeneously heated film in radial direction

The first effect is explained as the driving force for nanosecond-laser ablation [26]. However, in our simulation, where ultra-short pulses were used, the thermal expansion generated a pressure that was 5 orders of magnitude above the pressure from gas expansion under confinement. Thus, the gas pressure can be neglected and thermal expansion can be regarded as the driving force. The ultrafast thermal expansion produces a shock wave [32, 57, 58], which propagates to the upper air-side boundary and a recoil pressure which initiates the delamination process of the Mo film

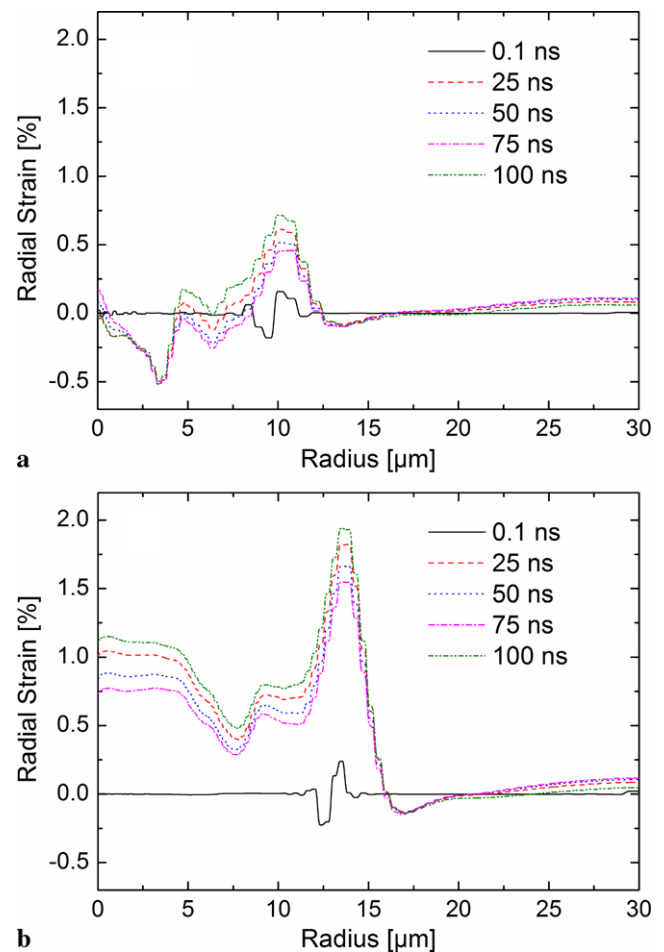


Fig. 16 Maximum values for radial strain (a) for 0.40 J/cm^2 and (b) for 0.55 J/cm^2 . The strain maximum appears at the edges of the confined melting radius. The strain level rises with higher fluence. Also a strain raise is visible at the centre, which can lead to a crack, as described by Heise et al. [16]

from the substrate within an area of the melting radius. The shock wave accelerates the Mo film, without a significant contribution from radial thermal stress. To accelerate the film to nearly constant velocity of about 30 to 50 m/s by a time of about 100 ps, a value in the order of 10^{11} multiple of g is required. Consequently, ultrafast expansion in axial direction is the main initial driving force. We further found that 1/3 of the impulse is generated by ultrafast heating and 2/3 by ultrafast melting [59]. The consequence is that “lift-off” occurs although the layer has not been molten completely. The simulation revealed that the maximum melting depth is only 1/4 of the of the layer thickness. In comparison, nanosecond laser ablation heats a larger volume with a lower heat rate and lower expansion rate. The back reaction is therefore too small to ablate the layer before melting and evaporation occurs. Evaporation may take over the major role in nanosecond processing, because a larger fraction of the layer is melted and because the vapour can absorb energy directly from the laser.

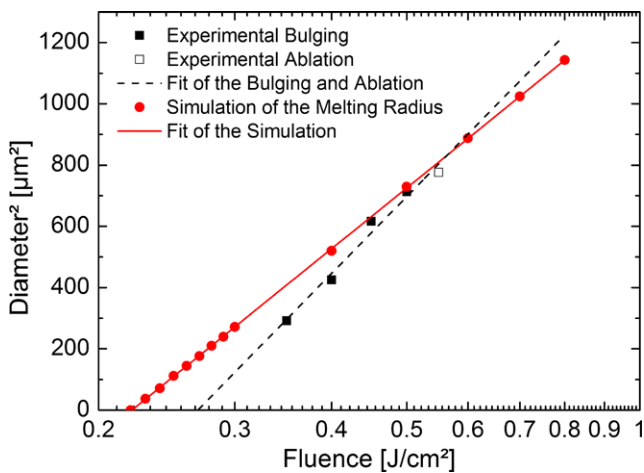


Fig. 17 Liu plot of the directly induced laser ablation

4.2 Comparison with experiment: ablation thresholds

The simulation has been conducted in accordance with the experimental parameters chosen in Ref. [32]. The first validation compares the simulated ablation area with the experimental results, using the method of Liu et al. [60]. In Fig. 17 the experimental values for the squared ablation diameter are plotted against the logarithm of the fluence [32]. In the experiment, for fluence of between about 0.3 and 0.5 J/cm², dome formation was observed and for fluence above 0.5 J/cm² a “lift-off” ablation was observed. For the simulation, the calculated melt diameter is plotted. Within this diameter the molybdenum is assumed to have lost most of its adhesion forces and separation from the glass substrate is allowed. At the fixed edges the maximum strain is observed.

Comparison between data and simulation shows a good agreement between calculated melt diameter and measured ablation diameter. For the slight, systematic disagreement, some explanations are possible: First, the melt diameter depends on the electron temperature model parameter, which are still under debate. Second, the temperature dependence of the light absorption coefficient has not been taken into account. The energy localization is probably even better leading to a better energy utilization and larger slope of the simulated Liu plot. Concerning the strain threshold for ablation, a strain value of 2 % is exceeded for 0.55 J/cm² in the simulation. This is then the criterion for fracture from simulation, deduced from comparison with experiment.

4.3 Comparison with experiment: pump-probe microscopy

With experimental pump-probe investigations, the dome height could be experimentally observed as a function of time [32]. Figure 18 illustrates the results and compares it with the simulated height in the centre position.

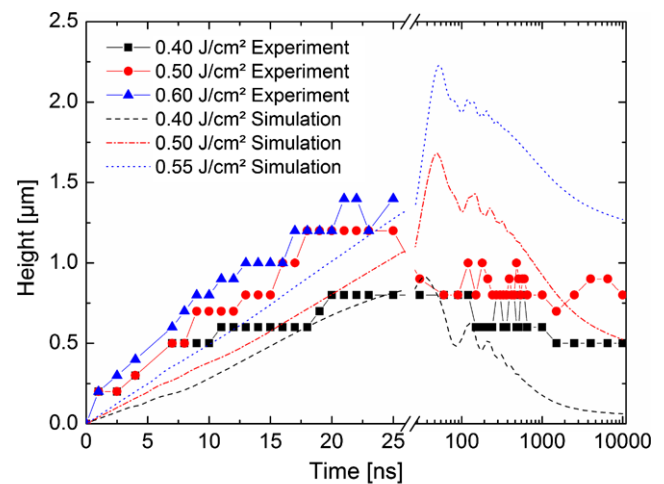


Fig. 18 Data of the dome height obtained from time resolved pump-probe investigations [32] compared with simulated results.

The overall agreement is very good. Due to the constant velocity after 1 ns, there is nearly no acceleration. This is in good agreement with the simulated average acceleration in Fig. 10. For 0.5 J/cm² the simulation predicts a membrane velocity of 40 m/s, while the experimental result shows a value of 60 m/s. The data furthermore show that the initial dome height is shrinking with time and that no dome has been measured for fluence larger than 0.50 J/cm². The estimated maximum static dome height of 970 nm for 0.40 J/cm² is consistent with the simulation and experimental results. For 0.50 and 0.60 J/cm² the estimation still fits to the experimental values, but the simulation height is too large, due to the insufficient modelling of the plastic parameters. The dome shrinking is related to the cooling until initial room temperature is reached. The remaining dome height is the result of plastic deformation.

The comparison shows that the membrane velocity is calculated to be too slow. The reason may be the simplification in the model for the volume expansion during melting, where the effect is smeared out over the melt volume instead of being localized forming a shock front. The reason for the deviation in dome height at later times could be explained from the unknown plastic behaviour of the sputtered molybdenum layer. Like all refractive vacuum coated metals, the material properties are not comparable with bulk and are probably very anisotropic. The plastic parameters have been estimated for our model only to demonstrate qualitatively the mechanism of dome formation and have not been fitted to reproduce the pump probe data exactly.

5 Conclusions

The presented model describes the mechanism of “directly induced” laser ablation of a thin Mo film on a glass substrate.

The model focuses on ultra-short laser pulse processes, with high energy efficiency. The energy for ablation is only one-tenth compared to a direct laser process and the damage related to excessive melting and evaporation is low. Because the laser energy is deposited ultrafast in a localized region near the interface, the Mo layer thermally expands fast and produces a shock wave initiating the ablation process. The expansion into the substrate produces a back reaction and creates large enough forces and strain for film bulging and ablation. Thermal expansion due to heating and melting must be assumed to get the right value for “lift-off”. Evaporation is not required in the mechanism and is observed for a very short time period. In addition, the produced vapour pressure is not large enough to get a significant mechanical effect. The insight gained in this investigation concerns the fundamental role of the backward impulse generated by the substrate for “directly induced” laser ablations leading to a “lift-off”. This produces a sufficiently high acceleration to set the layer in motion away from the substrate. The effect is therefore purely mechanical and the characterization is therefore “cold ablation”.

This insight has been made possible by a 3D axisymmetric multiphysics model extending over several decades in time and modelling the physical processes very accurately. In this model, the process and material parameters may be varied and investigated systematically as there are: the electronic and optic parameter of the materials, the elastic parameter of layer and substrate. Our model assumptions can explain all observed phenomena and magnitudes. In such a way, the “directly induced” laser ablation process may be improved. At the same time, the experimental validation can be improved using the discovered dependencies in the investigation.

Acknowledgements This work was partly funded by the Seventh Framework Programme of the European Commission within the project ‘SolarDesign’, under Grant No. 310220 and by the German Research Foundation within the Project ‘Modelling in Nanostructure Technology’, under the DFG-Number INST 99/10-1.

References

1. H.P. Huber, M. Englmaier, C. Hellwig, A. Heiss, T. Kuznicki, M. Kemnitzer, H. Vogt, R. Brenning, J. Palm, Proc. SPIE **7203**, 72030R (2009)
2. G. Heise, C. Hellwig, T. Kuznicki, S. Sarrach, C. Menhard, A. Heiss, H. Vogt, J. Palm, H.P. Huber, Proc. SPIE **7585**, 75850U (2010)
3. H. Vogt, A. Heiss, J. Palm, F. Karg, H.P. Huber, G. Heise, in *26th EUPVSEC 3DV2.9* (2011)
4. A. Burn, V. Romano, M. Muralt, R. Witte, B. Frei, S. Bücheler, S. Nishiwaki, Proc. SPIE **8243**, 824318 (2012)
5. P. Gecys, G. Raciukaitis, A. Wehrmann, K. Zimmer, A. Braun, S. Ragnow, J. Laser Micro Nanoeng. **7**, 33 (2012)
6. P.O. Westin, U. Zimmermann, M. Ruth, M. Edoff, J. Sol. Energy Eng. **95**, 1062 (2011)
7. G. Eberhardt, H. Banse, U. Wagner, T. Peschel, Proc. SPIE **7585**, 75850P (2010)
8. P. Gecys, G. Raciukaitis, M. Ehrhardt, K. Zimmer, M. Gedvilas, Appl. Phys. A **101**, 373 (2010)
9. F.J. Pern, L. Mansfield, S. Glynn, B. To, C. DeHart, S. Nikumb, C. Dinkel, M. Rekow, R. Murison, T. Panarello, C. Dunskey, in *35th IEEE Photovolt. Spec. Conf.*, vol. 5614717 (2010)
10. M. Rekow, R. Murison, C. Dunskey, C. Dinkel, J. Pern, L. Mansfield, T. Panarello, S. Nikumb, in *25th EUPVSEC 3DO.5.5*, (2010)
11. G. Heise, A. Heiss, C. Hellwig, T. Kuznicki, H. Vogt, J. Palm, H.P. Huber, Prog. Photovolt. Res. Appl. (2012). doi:[10.1002/pp.1261](https://doi.org/10.1002/pp.1261)
12. A.D. Compaan, I. Matulionis, S. Nakade, Opt. Lasers Eng. **34**, 15 (2000)
13. D. Bartl, A. Michalowski, M. Hafner, A. Letsch, S. Nolte, A. Tünnermann, Appl. Phys. A **110**, 227 (2013)
14. W.S. Wong, T. Sands, N.W. Cheung, M. Kneissl, D.P. Bour, P. Mei, L.T. Romano, N.M. Johnson, Appl. Phys. Lett. **77**, 2822 (2000)
15. G. Heise, J. Konrad, S. Sarrach, J. Sotrop, H.P. Huber, Proc. SPIE **7925**, 792511 (2011)
16. G. Heise, M. Domke, J. Konrad, S. Sarrach, J. Sotrop, H.P. Huber, J. Phys. D, Appl. Phys. **45**, 315303 (2012)
17. J. Bohandy, B.F. Kim, F.J. Adrian, A.N. Jette, J. Appl. Phys. **63**, 1158 (1988)
18. V. Schultze, M. Wagner, Appl. Surf. Sci. **52**, 303 (1991)
19. T.V. Kononenko, P. Alloncle, V.I. Konov, M. Sentis, Appl. Phys. A **94**, 531 (2009)
20. V. Menezes, K. Takayama, T. Ohki, J. Gopalan, Appl. Phys. Lett. **87**, 1 (2005)
21. G. Heise, D. Trappendreher, F. Ilchmann, R.S. Weiss, B. Wolf, H.P. Huber, Proc. SPIE **8247**, 82470X (2012)
22. S. Hermann, N.P. Harder, R. Brendel, D. Herzog, H. Haferkamp, Appl. Phys. A **99**, 151 (2010)
23. P. Engelhart, S. Hermann, T. Neubert, H. Plagwitz, R. Grischke, R. Meyer, U. Klug, A. Schoonderbeek, U. Stute, R. Brendel, Prog. Photovolt. Res. Appl. **15**, 521 (2007)
24. S. Rapp, M. Domke, M. Schmidt, H.P. Huber, LIM 2013. Phys. Proc. **41**, 727 (2013)
25. R. Fabbro, J. Fournier, P. Ballard, D. Devaux, J. Virmont, J. Appl. Phys. **68**, 775 (1990)
26. F.J. Adrian, J. Bohandy, B.F. Kim, A.N. Jette, P. Thompson, J. Vac. Sci. Technol. B **5**, 1490 (1987)
27. N.T. Kattamis, M.S. Brown, C.B. Arnold, J. Mater. Res. **26**, 2438 (2011)
28. T.E. Itina, J. Hermann, P. Delaporte, M. Sentis, Thin Solid Films **513**, 453–454 (2004)
29. D. Ivanov, B. Rethfeld, G. O’Connor, T. Glynn, A. Volkov, L. Zhigilei, Appl. Phys. A **92**, 791 (2008)
30. M.V. Shugaev, N.M. Bulgakova, Appl. Phys. A **101**, 103 (2010)
31. I. Zergioti, D.G. Papazoglou, A. Karaiskou, C. Fotakis, E. Gamaly, A. Rode, Appl. Surf. Sci. **177**, 208–209 (2003)
32. M. Domke, S. Rapp, M. Schmidt, H.P. Huber, Appl. Phys. A **109**, 409 (2012)
33. M. Domke, S. Rapp, M. Schmidt, H. Huber, Opt. Express **20**, 10330 (2012)
34. M. Domke, S. Rapp, H. Huber, Phys. Proc. **39**, 717 (2012)
35. M. Domke, S. Rapp, G. Heise, H.P. Huber, Proc. SPIE **8243** (2012)
36. A.P. Alloncle, R. Bouffaron, J. Hermann, M. Sentis, Proc. SPIE **6261**, 626127 (2006)
37. S. Beyer, V. Tornari, D. Gornicki, Proc. Inst. Mech. Eng. B **5063**, 202 (2003)
38. Q. Bian, X. Yu, B. Zhao, Z. Chang, S. Lei ICALAO **2011**, 869 (2011)

39. S. Preuss, A. Demchuk, M. Stuke, *Appl. Phys. A* **61**, 33 (1995)
40. S. Preuss, E. Matthias, M. Stuke, *Appl. Phys. A* **59**, 79 (1994)
41. G. Heise, M. Englmaier, C. Hellwig, T. Kuznicki, S. Sarrach, H. Huber, *Appl. Phys. A* **102**, 173 (2011)
42. R.S. Hixson, M.A. Winkler, *Int. J. Thermophys.* **13**, 477 (1992)
43. Comsol Multiphysics <http://www.comsol.com/>
44. S.I. Anisimov, B.L. Kapeliovich, T.L. Perelman, *Sov. Phys. JETP* **39**, 375 (1974)
45. J.K. Chen, D.Y. Tzou, J.E. Beraun, *Int. J. Heat Mass Transf.* **49**, 307 (2006)
46. J. Hohlfeld, S.S. Wellershoff, J. Güdde, U. Conrad, V. Jähnke, E. Matthias, *Chem. Phys.* **251**, 237 (2000)
47. S.S. Wellershoff, J. Hohlfeld, J. Güdde, E. Matthias *Appl. Phys. A* **69** (1999)
48. J. Huang, Y. Zhang, J.K. Chen, *Appl. Phys. A* **103**, 113 (2011)
49. M.M. Kirrilova, L.V. Nomerovannaya, M.M. Noskov, *Sov. Phys. JETP* **33**, 1210 (1971)
50. D.R. Lide, *CRC Handbook of Chemistry and Physics*, 84th ed. (CRC Press, Boca Raton, 2004)
51. L.D. Landau, E.M. Lifschitz, *Course of Theoretical Physics—Theory of Elasticity* (Butterworth, Stoneham, 1991)
52. COMSOL multiphysics user's Guide V 4.1 2010, 501 ff
53. R. Farraro, B.R. McLellan, *Metall. Trans. A* **8**, 1563 (1977)
54. C.W. Siders, A. Cavalleri, K. Sokolowski-Tinten, C. Toth, T. Guo, M. Kammler, M. Horn Von Hoegen, K.R. Wilson, D. Von Der Linde, C.P.J. Barty, *Science* **286**, 1340 (1999)
55. A. Barty, S. Boutet, M.J. Bogan, S. Hau-Riege, S. Marchesini, K. Sokolowski-Tinten, N. Stojanovic, R. Tobey, H. Ehrke, A. Cavalleri, S. Duesterer, M. Frank, S. Bajt, B.W. Woods, M.M. Seibert, J. Hajdu, R. Treusch, H.N. Chapman, *Nat. Photonics* **2**, 415 (2008)
56. M. Domke, J. Sotrop, S. Rapp, M. Börger, D. Felsl, H.P. Huber, *Proc. SPIE* **8611**, 861146 (2013)
57. A. Mermillod-Blondin, A. Rosenfeld, R. Stoian, E. Audouard, *Proc. SPIE* **8247**, 82470Q (2012)
58. E.G. Gamaly, *Phys. Rep.* **508**, 91 (2011)
59. B. Rethfeld, K. Sokolowski-Tinten, D. Von Der Linde, S.I. Anisimov, *Appl. Phys. A* **79**, 767 (2004)
60. J.M. Liu, *Opt. Lett.* **7**, 196 (1982)